Title

Mechanisms of graphite ablation by sub-millisecond ytterbium fiber laser pulses

Journal

Applied Physics Letters, 121(9)

ISSN

0003-6951

Authors

Park, Minok

Balkey, Matthew M

Mao, Xianglei

et al.

Publication Date

2022-08-29

DOI

10.1063/5.0109618

Mechanisms of graphite ablation by sub-millisecond ytterbium fiber laser pulses

Minok Park[1,2,3], Matthew M. Balkey[4], Xianglei Mao[1], Jacob C. Jonsson[5], Costas P. Grigoropoulos[2,3,*], and Vassilia Zorba[1,3,*]

[1]Laser Technologies Group, Energy Technologies Area, Lawrence Berkeley National Laboratory, Berkeley, California 94720, USA
[2]Laser Thermal Laboratory, Department of Mechanical Engineering, University of California at Berkeley, Berkeley, California 94720-1740, USA
[3]Department of Mechanical Engineering, University of California at Berkeley, Berkeley, California 94720-1740, USA
[4]Sandia National Laboratories, PO Box 5800, Mail Stop 0791, Albuquerque, New Mexico 87185-0791, USA
[5]Windows & Envelope Materials Group, Energy Technologies Area, Lawrence Berkeley National Laboratory, Berkeley, California 94720, USA

[*]Authors to whom correspondence should be addressed: cgrigoro@berkeley.edu and vzorba@lbl.gov

Abstract

Graphite is a key material in a variety of cross-cutting applications in energy conversion, energy storage, and nuclear energy. Recently, temporally modulated CW lasers have been shown to produce well-defined ablation features in graphite at relatively high processing speeds. In this work, we analyze in detail the laser ablation dynamics of single-pulse ablation in the sub-millisecond time regime to elucidate the origins of the resulting well-defined ablation craters using a combination of time-resolved emission imaging, diffuse reflection/scattering imaging, and optical emission spectroscopy. These multi-modal *in situ* diagnostics revealed three main contributors to achieving well-defined ablation features: (1) rapid ejection of particles with ~100 m/s speed, (2) ablation of the graphite in the gaseous form, and (3) absence of bulk liquid motion which is typically observed in laser processing of metals. Plasma plume formation was sustained throughout the duration of the laser pulse (500 μs). This work provides insights into the complex physical and chemical mechanisms of sub-millisecond laser-matter interactions, which are critical for parameter space optimization and tailoring of laser machining and drilling processes.

Graphite plays a prominent role in the development of new materials in a variety of applications such as emitters for thermophotovoltaics[1, 2], absorbers for solar water desalination[3], and anodes for lithium-ion-batteries[4, 5] due to the combination of outstanding performance and low material cost. Prior to use in such applications, pristine graphite is often machined, drilled, or cut into pieces by mechanical abrasive tools.[6] However, these methods fail to provide high machining quality, and abrasive tools are easily worn. Alternatively, laser ablation processes by pulsed lasers have been proposed for patterning, drilling, and machining graphite due to the confined energy deposition which produces precise ablated features in $O(10\ \mu m)$ length scales[4, 7-10]. Nevertheless, processing in wafer-size scales using such lasers is time-consuming and hence undesirable for scaled-up manufacturing.

Temporally modulated continuous wave (quasi-CW) fiber lasers were recently introduced as means to machine graphite at large ablation depths via single pulse irradiation[11], which translates to rapid processing rates. More importantly, the resulting ablation features on graphite are well-defined, free of undesirable burrs or re-solidified/deposited residues which are spontaneously formed during the prolonged laser-material interaction in metals[12-16]. However, the origin of this behavior remains unknown. Since the laser-matter interaction in the tens of microseconds to sub-millisecond pulse regime is largely unexplored there is a need for systematic studies into the mechanisms of plasma expansion and chemistry in this time regime to elucidate, improve, and tailor the resulting surface features on graphite.

In this Letter, we used a suite of multimodal diagnostics to analyze the ablation dynamics of graphite induced by a single sub-millisecond laser pulse from a CW ytterbium (Yb) fiber laser. Emission imaging across the 500-930 nm spectral range under two different viewing angles (45° and 90°) was utilized to study the ejection of graphite particles and plasma plumes. *In situ* diffuse reflection/scattering imaging with a probe laser was also used under two observation angles to investigate ablation mechanisms in the vicinity of the graphite surface, and to probe the evolution of the laser-induced craters during the single pulse. Emission and reflection/scattering imaging were complemented

by optical emission spectroscopy, which was provided information about the chemical composition of the expanding laser-induced plasmas. In addition to the *in situ* diagnostics described above, we studied the sample topology and optical properties *ex situ,* before and after ablation. The combination of advanced multimodal *in situ* diagnostics with *ex situ* surface morphology characterization provides insights into the physics and chemistry of single-pulse ablation of graphite with temporally modulated CW fiber lasers.

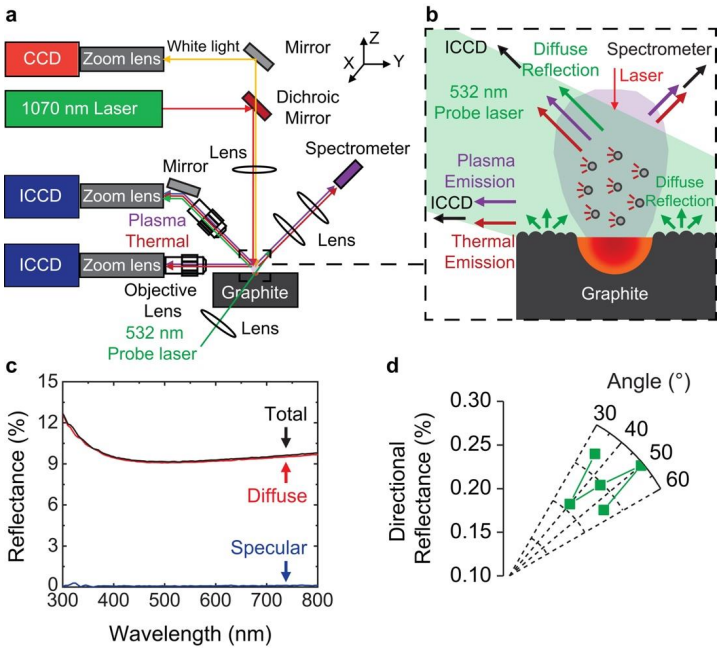

Figure 1. (a) Optical setup for time-resolved emission and diffuse reflection imaging with an ICCD camera. The long pulse laser (1070 nm, 500 μs) irradiated the sample graphite surface in the normal direction. A 532 nm CW probe laser was used for time-resolved diffuse reflection/scattering imaging under two observation angles (45° and 90°). Thermal- and plasma-induced emission were imaged (500 – 930 nm) under two viewing angles and also spectrally analyzed with optical emission spectroscopy. (b) Detailed schematic of techniques used to probe the plasma plume, particles, and the surface. (c) *Ex situ* measurement of total, diffuse, and specular reflectance of the graphite specimen prior to laser processing, measured by a UV – VIS spectrophotometer. (d) *Ex situ* measurement of directional reflectance of the graphite at 532 nm wavelength, acquired using FTIR prior to laser processing.

Figure 1 (**a**) shows the optical setup used to study the ablation mechanisms of graphite in air under atmospheric conditions. Specifically, single pulses (500 μs pulse duration, 1070 nm wavelength, and $M^2 = 1.05$ beam quality) of the Yb fiber laser (YLR-150/1500-QCW-AC, IPG Photonics) were focused by a convex lens (f = 150 mm) on fresh locations of the sample at a normal angle of incidence, yielding a 30 μm beam diameter. A laser peak power of 280 W (= 3.96×10^7 W/cm^2) was used in this work. Graphite substrates of 0.5 mm in thickness (purity 99.95 %, fine grain size, Goodfellow) were used as targets.

To investigate the dynamics of ejecta up to the near-infrared spectral range, we implemented time-resolved emission imaging and *in situ* diffuse reflection/scattering imaging with a 532 nm CW probe laser (Laserglow Technologies), coupled with a 10× objective lens (Mitutoyo), a 12× zoom lens (Navitar), and an Intensified Charged Coupled Device (ICCD) camera (PI-MAX2, Princeton Instruments) at different times after the laser pulse. We selected

532 nm as the probing wavelength because it does not interfere with the C_2 / CN plasma emission bands observed with optical emission spectroscopy.

In addition to the *in situ* diagnostics described above, we studied *ex situ* the sample before and after ablation with a single sub-millisecond pulse. The sample surface morphology was characterized prior to and following laser irradiation using white light interferometry (WLI) and scanning electron microscopy (SEM). Furthermore, we used UV – VIS spectrophotometry (Lambda 950, Perkin-Elmer) with a 150 mm integrating sphere to measure the total, diffuse, and specular reflectance of the pristine graphite sample, as well as Fourier Transform Infrared Spectrometer (FTIR) (Nicolet iS50, Thermo Fisher) with an accessory kit to measure directional reflectance at specific wavelengths of interest. The latter provided information for the design of the *in situ* diffuse reflection/scattering imaging with the 532 nm CW probe laser.

In designing of the *in situ* diffuse reflection/scattering imaging, we had to factor in the roughness of the uneven graphite surface (Fig. S1). For surface roughness which falls under the geometric regime (i.e., $\sigma_{rms} / \lambda > 1$)[17], the directional reflection distribution of the incident light is dependent on the surface morphology. Here, σ_{rms} is the RMS surface roughness, and λ is the irradiation wavelength. Due to the higher sample surface roughness (σ_{rms} = 1.313 μm – Fig. S1) compared to the probing wavelength (λ = 532 nm), the probe laser is reflected diffusely (9.1 %) rather than specularly (< 0.1 %), as verified with UV-VIS spectrophotometry presented in **Fig. 1 (c)**. Diffuse reflection enables us to observe the surface *in situ* under 532 nm laser illumination, even though the directional reflectance at 45° was measured as only ~ 0.25 % (**Fig. 1 (d)**). Accordingly, the probing laser was loosely focused on the graphite surface via a convex lens (f = 100 mm), fully covering the field of view of the ICCD camera. The optical power of the probe laser was fixed at 1.0 W to prevent pixel saturation.

Time-resolved emission imaging was performed on the same setup but without the probing laser, to examine emission from plasma plumes and the thermal emission from graphite in the 500-930 nm spectral range filtered by a spectral bandpass filter (FESH0950, Thorlabs). Optical emission spectra were acquired to correlate ejection dynamics with plasma chemistry. Spectral emission was collected by two convex lenses at 45° and focused onto an optical fiber coupled to a spectrometer (IsoPlane, Princeton Instruments) equipped with an ICCD camera (PI-MAX3, Princeton Instruments). Flat field correction was performed on all of the collected emission spectra.

The ICCD temporal resolution (i.e., gate width) was adjusted in the range of 200 ns – 5 μs to match the timescale of the relevant material ejection processes. 0.33 μs was the shortest gate delay with respect to when the laser irradiation hit the surface, due to the synchronization between the diagnostic system components and the pump laser, which limits studying the early plasma expansion dynamics before 0.33 μs. To ensure consistency and reproducibility, each measurement was performed at a fresh sample location.

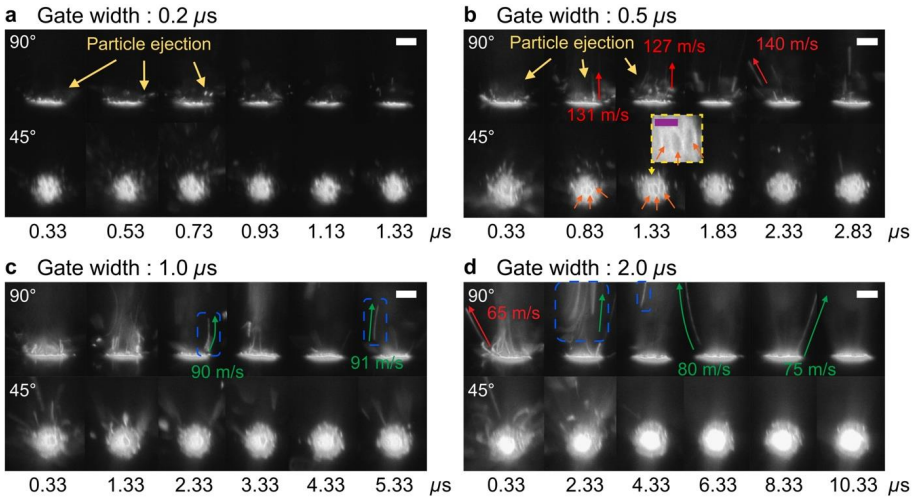

Figure 2 Time – resolved emission imaging was performed to analyze early-phase material ejection up to 10.33 μs gate delay. Images were acquired for (a) 0.2 μs, (b) 0.5 μs, (c) 1.0 μs, and (d) 2.0 μs gate width, respectively, under varying gate delay. Two different angles (90° and 45° angle with respect to the surface) were employed to observe the target surface. The colored arrows (red / green) show different types of ejecta moving at varying speeds. The white scale bar is 50 μm, and the purple scale bar is 25 μm.

Figure 2 shows the early ablation dynamics examined via time-resolved emission imaging acquired for different gate width (0.2 μs – 5 μs) at two different observation angles. Specifically, a side probing angle (90°) was chosen to examine the plasma plume and particle ejection, while a viewing angle (45°) was employed to observe the graphite surface phenomena *in situ*. Fig. S2 shows the spectral decomposition of emission images.

Based on side imaging (90°) in **Fig. 2** and Fig. S2, particles evidenced by bright streak-lines which were ejected as early as at 0.33 μs time delay after the laser pulse first hits the surface (**Fig. 2 (a) – (b)**), and continued to be ejected until ~ 6 μs gate delay (**Fig. 2 (d)**). The velocities of the ejecta were calculated based on the travel lengths (red, and green arrows) over the corresponding gate widths. At delays longer than 6 μs, evidence of particle ejection was diminished, while plasma plume and blackbody radiation emission were mainly observed (more information in **Fig. 3**).

The time-resolved graphite surface images captured irregular ablation events (**Fig. 2 (b)**). In particular, ring-shaped ejecta were released from the surface (marked by orange arrows and enlarged in the yellow box at the 45° images), at ~130 m/s speed (indicated by red arrows in the 90° snapshots). In the case of aluminum (Al) irradiated under identical conditions, particles observed at ~ 2 μs gate delay were produced from the breakup of ejected liquid column jets when high kinetic energy overcame surface tension.[13] However, we could not observe such liquid material ejection for the case of graphite under single sub-millisecond pulse irradiation. Instead, particles were directly expelled from the bulk substrate (side imaging in **Fig. 2**). Hence, it is likely that the ejected graphite particles originate from spallation or fragmentation processes rather than molten-liquid mediated removal such as breakup from the liquid jet or thermo-capillary ejection.

Furthermore, the ejected particles could be distinguished into two types: (1) particles escaping sideways from the irradiated spot at > 65 m/s speed (e.g., red arrow, 0.33 μs delay in **Fig. 2 (d)**), and (2) particles ejected within the emitted plumes (green arrows with blue boxes, **Fig. 2 (c) – (d)**). Particles of type 1 propagated outward and disappeared from the field of view. However, the trajectories of type 2 particles shifted towards the central region and followed the plume ejection direction (blue boxes). Previous work on femtosecond laser ablation showed that particle momentum decreases continuously after the initial release (~ 1.7 μs delay) due to the presence of ambient air and the lack of a sustaining thrust.[18] However, in this work we find that the speed of graphite particles exceeds 75 m/s even after 2 μs delay as indicated by scattering imaging (green arrows). Therefore, we believe that the vertical motion of graphite particles at > 2 μs delay would be further driven by the upstream plume whose flow speed is ~80 m/s (**Fig. 2 (c) – (d)**), after the initial release. This behavior results in the rapid particle removal from the surface and minimal re-deposition as evidenced by corresponding clean and well-defined ablation crater morphologies (**Fig. 5 (a)**).

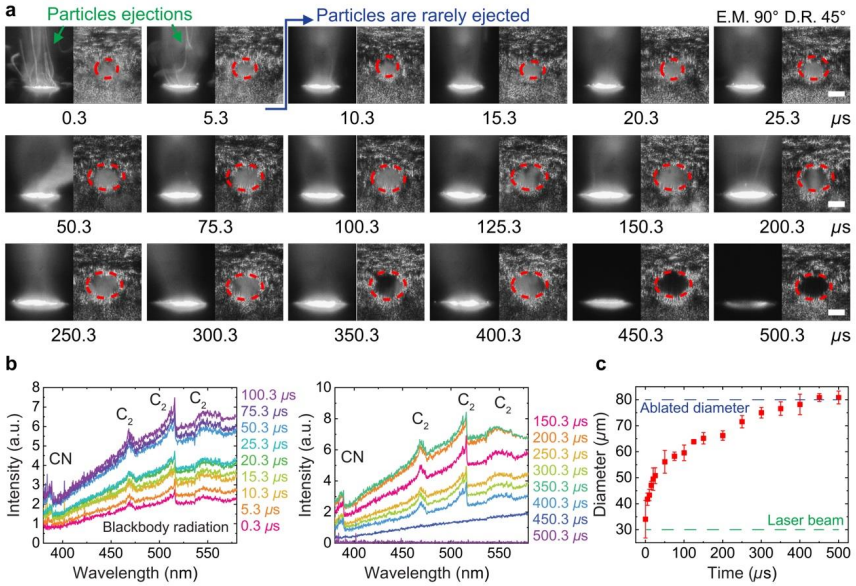

Figure 3 (a) Time – resolved emission images juxtaposed with diffuse reflection/scattering images acquired for 5 μs gate width. Emission (E.M.) images are shown under side viewing angle (90°) and diffuse reflection (D.R.) images under 45° viewing angle. The white scale bar is 50 μm. (b) Time – resolved optical emission spectra measured for 5 μs gate width at each time delay. (c) Growth of the ablation crater diameter vs. time extracted from diffuse reflection images shown in (a).

Figure 3 (a) shows time-resolved emission images acquired for 5 μs acquisition time under side view (90 °) together with the corresponding diffuse reflection images under tilted view (45 °) to probe the ablation dynamics at longer times and up to 500.3 μs gate delay. **Fig. 3 (b)** presents the time-resolved optical emission spectra measured for 5 μs at each time delay. Emission images taken under 45° angle are shown in Fig. S3.

As discussed in **Fig. 2**, particles which might experience a fragmentation process were removed from the surface at the early ablation phase (0.33 μs delay), while such particle ejection was barely observed after 10 μs gate delay. In addition to direct plasma emission imaging, we studied the time-resolved optical emission spectra across the 380-580 nm range, as shown in **Fig. 3 (b)**. We observed optical emission consisting of continuum, diatomic carbon C_2 (450 nm – 570 nm), and carbon nitride (CN) emission (384 nm – 389 nm). Diatomic carbon was detected from the $\Delta\upsilon = 1, 0, -1$ vibrational sequences of the C_2 Swan system[19, 20], and carbon nitride emission corresponded to the CN violet band ($B^2\Sigma^+ - X^2\Sigma^+$, $\Delta\upsilon = 0$)[21]. The origin of CN emission is attributed to the interaction of the expanding graphite plasma with N_2 in the atmosphere. Although we were not able to probe the early plasma expansion dynamics before 0.33 μs delay due to the limitation of synchronization, plasma plume formation continued during the laser material interaction for the duration of the pulse (500 μs), as verified in **Fig. 3 (b)**.

Based on the spectral emission data shown in **Fig. 3 (b)** combined with emission images in **Fig. 3 (a)**, we conclude that the majority of the ejecta in **Fig. 3 (a)** were upstream plasma plumes (C_2 and CN) without footprints of ejected particles. These results indicate that the graphite is ablated in gaseous form after approximately 10 μs. The lack of prominent particle generation may also be another key reason for the production of well-defined ablation features as shown in **Fig. 5 (a)**.

The time-dependent size variation of the laser ablation diameters is measured from the diffuse reflection/scattering images under 45º (**Fig. 3 (a)**), and these results are presented in **Fig. 3 (c)**. For this, 4 different scattering images were averaged at each time delay. We find that the diameter growth rate, decreases exponentially over the duration of the pulse and reaches plateau after 400 μs delay.

As expected, diffuse reflection imaging did not capture liquid phase motion after 100 μs delay, in contrast to Al ablation[13] under identical temporal modulation conditions, where a molten Al liquid pool was formed and oscillated over the surface, leading to the detachment of large droplets of $O(100\ \mu m)$ diameter. Accordingly, we infer that the absence of molten liquid pool is another contributing factor to the well-defined ablated features observed on graphite (see **Fig. 5 (a)**).

Thermal radiation is emitted from a body due to its temperature.[22] Examining in more detail the emission images filtered at 532 nm at early times (0.33 μs gate delay, Fig. S2 (b)), we find that continuum emission predominantly originates from the target specimen as no emission is detected from the plasma above the surface. Therefore, we conclude that continuum emission over the duration of the laser irradiation time (500 μs) comes predominantly from thermal radiation, resulting from heating of the graphite surface at elevated temperatures (see emission images in **Fig. 3 (a)**).

Based on this, we estimated the surface temperature by fitting Planck's blackbody radiation distribution to the optical emission spectra. This information is shown in **Fig. 4** (see details in Fig. S4 (a)).[22] For this, 10 emission spectra were averaged at each time delay. We found that after laser irradiation, the surface temperature reached a peak temperature of ~ 4050 K at 10 μs delay. After 10 μs, the temperature monotonically decreased until the expiration of the single laser pulse (500 μs).

Additionally, thermal emission to the ambient was back-calculated from the estimated temperatures (right axis in **Fig. 4**, and see derivations in Fig. S4 (b)).[22] During laser irradiation, thermal radiative loss was negligible (< 0.1 W) compared to the imparted laser power (280 W), indicating that the absorbed laser energy was mainly either dissipated to the bulk via heat conduction or used for vaporizing the graphite.

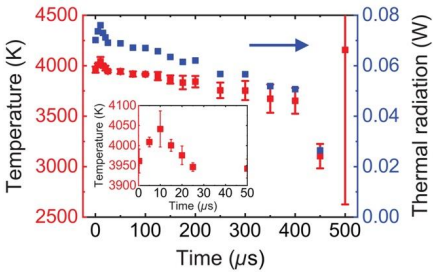

Figure 4 Time-resolved surface temperature of graphite following irradiation as estimated from emission spectra in Fig. 3 (b) via fitting Planck's blackbody radiation. Thermal emission to the ambient (right axis) was calculated from the average temperatures.

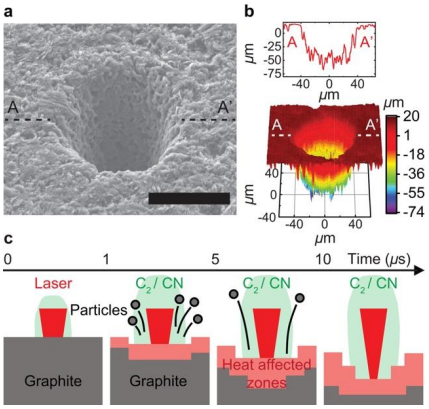

Figure 5 *Ex situ* surface morphology characterization of the graphite surface by (a) SEM, and (b) WLI, respectively. The scale bar is 50 μm. (c) Summarized ablation dynamics of graphite ablation induced by a temporally modulated Yb fiber laser.

Fig. 5 (a) – (b) shows *ex situ* characterization of surface morphology after the laser pulse with SEM and WLI. After single shot irradiation, the graphite ablation crater was 40 μm in radius and 60 μm in depth (below the original surface). Based on the experimental results discussed in **Fig. 2** to **Fig. 4**, the time-resolved ablation dynamics of graphite induced by a 500 μs Yb fiber laser pulse are summarized in **Fig. 5 (c)**. During the early phase ablation process before 6 μs, graphite particles were expelled from the surface at > 100 m/s ejection speeds via fragmentation of the target specimen. Subsequently, the released particles were entrained and swept by the upstream ejected plume at a speed of ~80 m/s. After 10 μs delay, emission from C_2 and CN as well as thermal radiation were observed without any evidence of bulk liquid motion on the surface.

In conclusion, we studied in detail the ablation mechanisms of graphite induced by a single Yb fiber laser pulse to elucidate the origin of the well-defined machined features. Time-resolved emission and diffuse reflection/scattering imaging at different observation angles enabled us to probe *in situ* the target surface as well as the ejected particles and plasma plumes. In particular, diffuse reflection imaging revealed the evolution of the laser-induced craters within the duration of the pulse. Optical emission spectroscopy offered information about the chemistry of plasma plumes and the transient surface temperature of graphite. The resulting laser ablation craters were well-defined without evidence of strong melting and resolidification phenomena. Three main factors can explain the well-defined ablation features: (1) sustained rapid removal of particles with ~100 m/s ejection speeds, (2) ablation of the graphite in the gaseous form, and (3) absence of liquid-mediated bulk motion. Plasma plume formation was sustained throughout the duration of the laser pulse (500 μs). These findings contribute towards comprehensive understanding of ablation mechanisms by modulated CW fiber laser and help select optimal laser processing conditions to improve the ablation efficiency as well as quality of machining and drilling in related applications.

Supplementary material

See supplementary material for surface morphology of the pristine graphite (Fig. S1), spectral decomposition of emission imaging (Fig. S2), time-resolved emission and diffuse reflection imaging at the tilted angle (45°) (Fig. S3), and derivation of transient temperature of graphite and calculation of blackbody radiation from the surface (Fig. S4).

Acknowledgement

This work was supported DOE NNSA – NA80 - Agreement # CT8405010 FUND CODE 01551 a grant through Sandia National Laboratories. This work was also supported by the US Department of Energy, Office of Defense Nuclear Nonproliferation Research and Development under contract number DE-AC02-05CH11231 at the Lawrence Berkeley National Laboratory. The authors thank Applied Spectra Inc., for use of one of their ICCD cameras.

PLEASE CITE THIS ARTICLE AS DOI: 10.1063/5.0109618

AUTHOR DECLARATIONS

Conflict of Interest

The authors have no conflicts of interest to disclose.

Data Availability

The data that support the findings of this study are available from the corresponding authors upon reasonable request.

Reference

1. Z. Omair, G. Scranton, L. M. Pazos-Outón, T. P. Xiao, M. A. Steiner, V. Ganapati, P. F. Peterson, J. Holzrichter, H. Atwater and E. Yablonovitch, Proceedings of the National Academy of Sciences **116** (31), 15356 (2019).
2. T. C. Narayan, L. Y. Kuritzky, D. P. Nizamian, B. A. Johnson, E. J. Tervo, A. R. Young, C. Luciano, M. K. Arulanandam, B. M. Kayes, E. E. Perl, M. Limpinsel, P. Santhanam, J. Slack, W. Olavarria, J. Carapella, M. Young, C. L. Wu, Z. J. Yu, Z. C. Holman, R. R. King, M. A. Steiner, D. M. Bierman, A. J. Ponec and J. A. Briggs, presented at the 2020 47th IEEE Photovoltaic Specialists Conference (PVSC), 2020 (unpublished).
3. W. Guan, Y. Guo and G. Yu, Small **17** (48), 2007176 (2021).
4. J. B. Habedank, J. Endres, P. Schmitz, M. F. Zaeh and H. P. Huber, Journal of Laser Applications **30** (3), 032205 (2018).
5. V. A. Agubra and J. W. Fergus, Journal of Power Sources **268**, 153-162 (2014).
6. Y.-K. Yang, M.-T. Chuang and S.-S. Lin, Journal of Materials Processing Technology **209** (9), 4395-4400 (2009).
7. M. D. Shirk and P. A. Molian, Carbon **39** (8), 1183-1193 (2001).
8. M. Luetke, V. Franke, A. Techel, T. Himmer, U. Klotzbach, A. Wetzig and E. Beyer, Physics Procedia **12**, 286-291 (2011).
9. J. Hoffman, Journal of Physics D: Applied Physics **48**, 235201 (2015).
10. J. Hoffman, J. Chrzanowska, S. Kucharski, T. Moscicki, I. N. Mihailescu, C. Ristoscu, and Z. Szymanski, Applied Physics A **117**, 395 (2014).
11. T. Doualle, M. Reymond, Y. Pontillon and L. Gallais, Applied Physics A **127** (9), 722 (2021).
12. S. Ly, G. Guss, A. M. Rubenchik, W. J. Keller, N. Shen, R. A. Negres and J. Bude, Scientific Reports **9** (1), 8152 (2019).
13. M. Park, M. M. Balkey, X. Mao, C. P. Grigoropoulos and V. Zorba, Applied Physics Letters **119** (22), 224103 (2021).
14. J. Tu, A. G. Paleocrassas, N. Reeves and N. Rajule, Optics and Lasers in Engineering **55**, 275-283 (2014).
15. D. W. Bäuerle, *Laser Processing and Chemistry*, 4 ed. (Springer-Verlag Berlin Heidelberg, 2011).
16. C. P. Grigoropoulos, *Transport in Laser Microfabrication: Fundamentals and Applications*. (Cambridge University Press, 2009).
17. C.-D. Wen and I. Mudawar, International Journal of Heat and Mass Transfer **49** (23), 4279-4289 (2006).
18. M. Park, J. Jeun, G. Han and C. P. Grigoropoulos, Applied Physics Letters **116** (23), 234105 (2020).
19. C. G. Parigger, J. O. Hornkohl, A. M. Keszler and L. Nemes, Appl. Opt. **42** (30), 6192-6198 (2003).
20. A. Arshad, S. Bashir, A. Hayat, M. Akram, A. Khalid, N. Yaseen and Q. S. Ahmad, Applied Physics B **122** (3), 63 (2016).
21. Y. Yamagata, A. Sharma, J. Narayan, R. M. Mayo, J. W. Newman and K. Ebihara, Journal of Applied Physics **86** (8), 4154-4159 (1999).
22. M. Q. Brewster, *Thermal Radiative Transfer and Properties*. (Wiley, 1992).

Applied Physics Letters

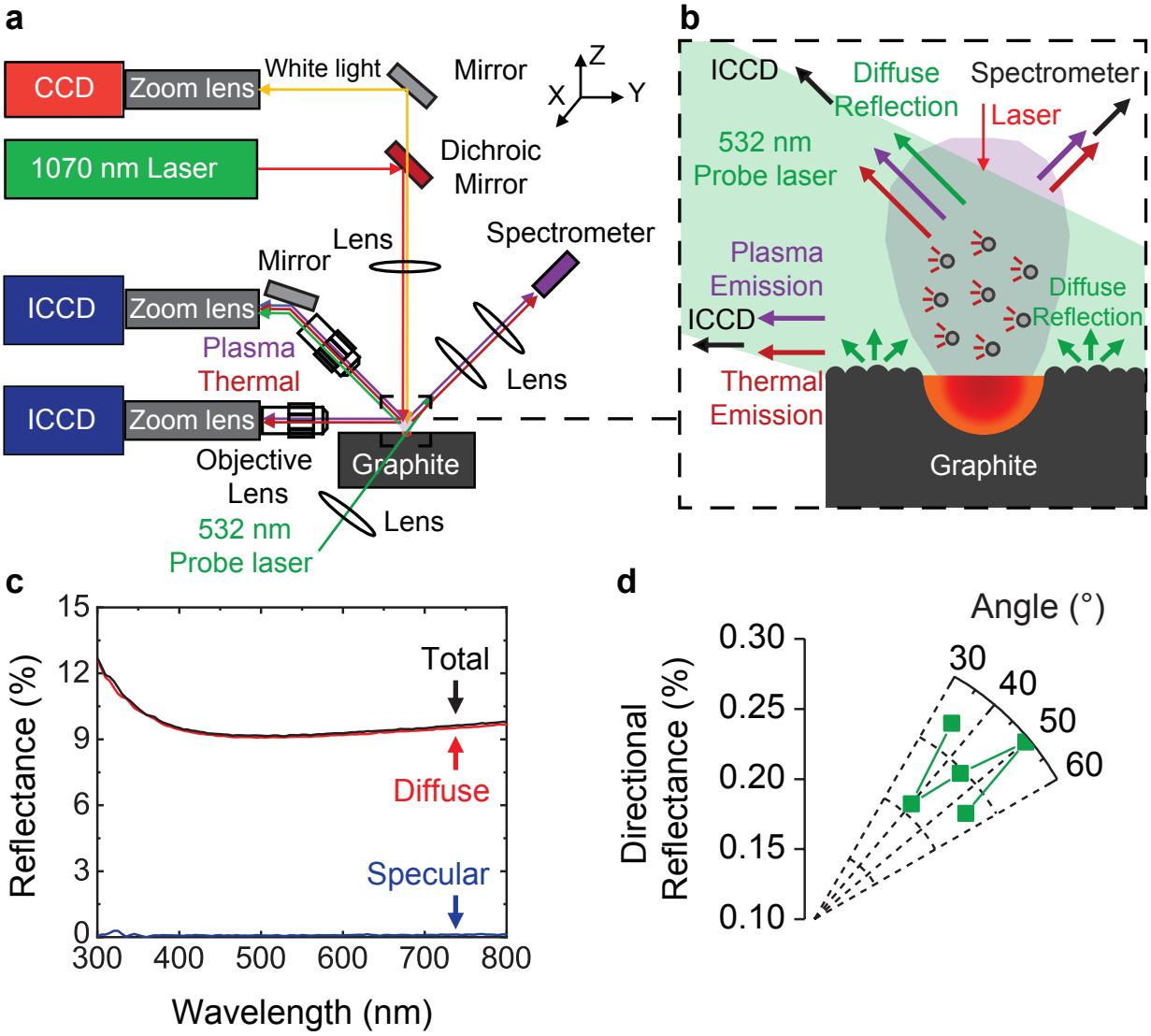

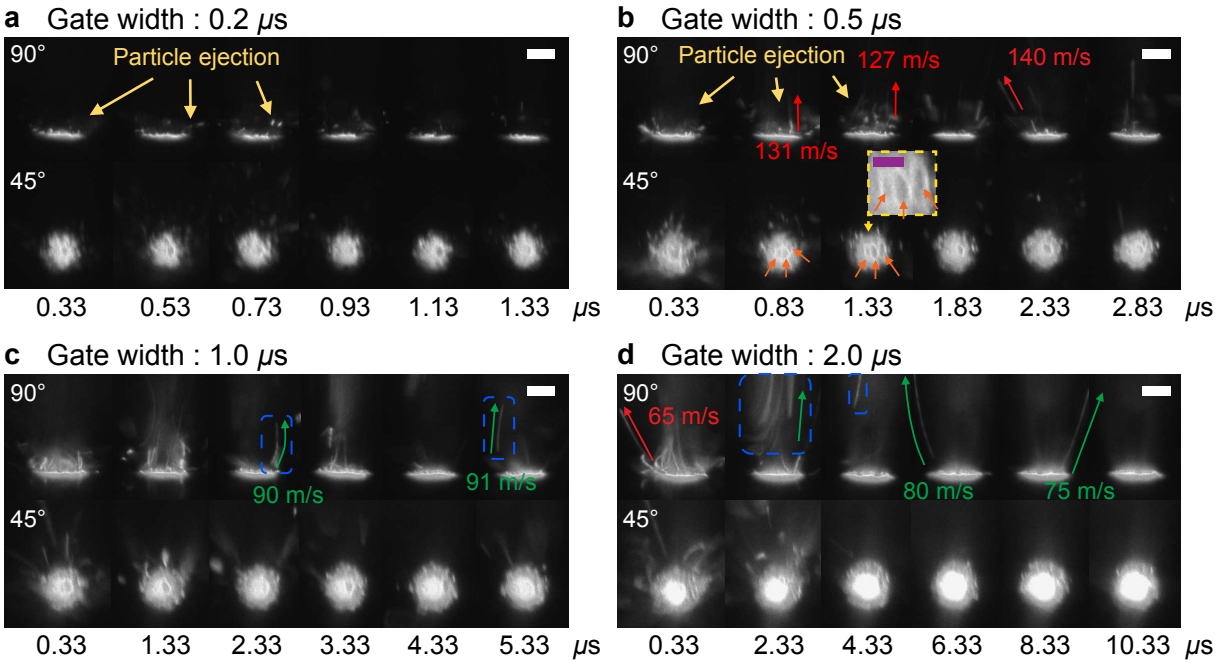

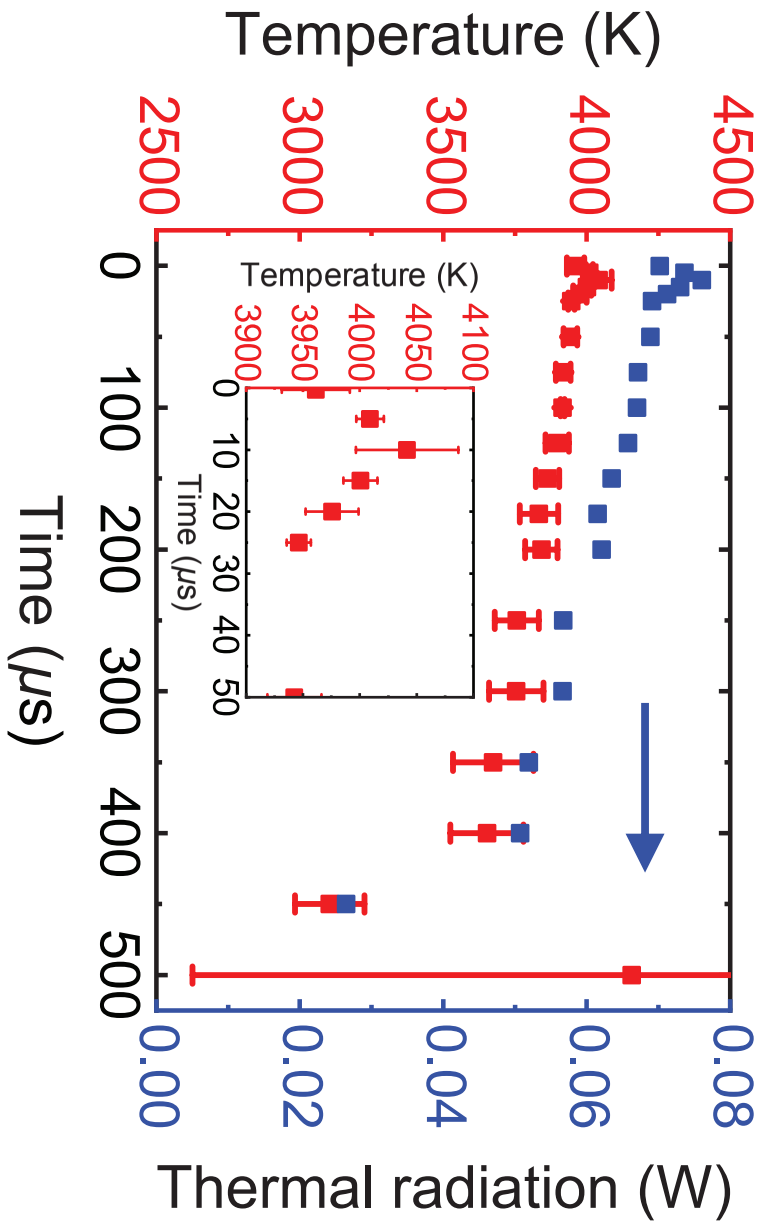

Applied Physics Letters

PLEASE CITE THIS ARTICLE AS DOI: 10.1063/5.0109618